



A computational study of the deposition of firebrands between two side-by-side blocks

Aditya Mankame, Patrick Damiani, Babak Shotorban *

Department of Mechanical and Aerospace Engineering, The University of Alabama in Huntsville, Huntsville, AL 35899, USA

ARTICLE INFO

Keywords:

Wildland-urban interface fires
Firebrands
Lagrangian tracking
Large eddy simulation

ABSTRACT

The deposition of firebrands between two blocks, representing neighboring simplified structures, was investigated by large-eddy simulation and Lagrangian tracking of firebrands. Fire Dynamics Simulator was modified and implemented for simulations. The computational configuration resembled the previous wind-tunnel measurement setup including two blocks and the firebrand generator apparatus, aka NIST Dragon (Suzuki and Manzello 2021). Different wind speeds and frictional coefficients between the sliding firebrands and the ground were considered. Simulations revealed several flow effects influencing the motion of firebrands on the ground, such as re-circulation flow in the wake of the dragon, a crossflow upwind of the blocks, and twin re-circulation regions on leeward and windward sides of the blocks. At lower wind speeds, firebrands were accumulated somewhere between the dragon and the blocks, consistent with observations in the previous measurements. At higher wind speeds, the firebrands tended to accumulate momentarily before the crossflow region and then accelerate through the gap between the blocks. Some accumulated in the leeward corner of the blocks. Firebrands displayed much more dispersion in the streamwise direction compared to the spanwise direction because the normal component of the Reynolds stress was greater in the streamwise direction.

1. Introduction

Wildland-urban interface (WUI) fires can cause extensive damage to both urban settlements and natural ecosystems. A common mechanism for their spread is spotting, which is caused by firebrands, namely airborne burning embers. Firebrands are generated by primary fires, and when deposited on flammable materials, they can initiate secondary fires, also known as spot fires. Firebrands travel short or long distances depending on their mass, shape, etc and the primary fire plume and wind conditions [1,2]. In WUI fires, they can land in proximity to a structure, igniting a spot fire that poses a threat to the structure from outside, or they can directly ignite the structure by landing on the structure, namely the roof [3,4].

Several measurement studies were conducted to investigate the role of firebrands in the WUI fire spread, using NIST Dragon [5] for the generation of firebrands. Manzello and Suzuki [5] studied the accumulation of firebrands on a decking assembly, and observed that wood decks were vulnerable to ignition from continuous, wind-driven firebrand showers. Suzuki et al. [6] and Manzello et al. [7] investigated the ignition of mulch beds by firebrands and the building component ignition vulnerability from mulch beds attacked by firebrand showers. Further investigations by Suzuki and Manzello [8] revealed that wood decking assemblies may be ignited within similar time to mulch

under certain conditions. In another set of experiments, Suzuki and Manzello [9] released firebrands upwind of two blocks in a parallel arrangement, and observed that at lower wind speeds, firebrands were accumulated in a zone between the blocks and the dragon. At higher wind speeds the firebrands slowed down in front of the blocks, but eventually slid out of the experimental area after passing the gap between the blocks.

Additional experimental and computational investigations were performed to specifically study the firebrand deposition. Tohidi and Kaye [10,11] conducted experimental and numerical studies to investigate the lofting of firebrands in a wind tunnel in an attempt to replicate the firebrand release into a wind from a convective plume. They tracked the released non-burning firebrands from the plume to its deposition and found that for higher wind speeds, the change in the initial vertical velocity of the plume did not affect the height or the landing distance of the firebrands. Nguyen and Kaye [12] conducted wind tunnel experiments on scaled-down building models to study firebrand accumulation on roofs. They found that most firebrands blown onto roofs were carried away by the wind, while those that remained tended to collect in internal roof corners. Firebrand accumulation decreased with higher wind speeds. In addition, they performed similar tests [13] involving multiple buildings around a target one and discovered that

* Corresponding author.

E-mail address: babak.shotorban@uah.edu (B. Shotorban).

upwind buildings of the target and with smaller separations increased firebrand mass on the target building's roof, linked it to flow characteristics. Anand et al. [14] conducted numerical studies on non-burning cylindrical firebrands released into turbulent flow over an open field, considering translational and rotational motions. They found that the deposited firebrands exhibited a spatial distribution resembling a bivariate Gaussian function, with a larger variance in the streamwise direction as compared to the spanwise. Anand [15] performed a similar study on burning firebrands, revealing that higher density ones experienced greater mass loss but retained more thermal energy upon landing compared to lower density counterparts. Mankame and Shotorban [16] simulated field-scale scenarios with firebrands released onto a single cubical structure, identifying a safe zone leeward of the structure where no firebrands were deposited. The length of this zone in the streamwise direction was proportional to the structure's height. Using a similar approach, Mankame and Shotorban [17] simulated the release of firebrands onto multiple cubic structures in tandem and parallel arrangements at varying wind speeds and observed formation of safe zones on the leeward side of all structures. At higher wind speeds and smaller separation distance in a tandem arrangement the safe zones extended on to the windward face of the trailing structure.

In view of above, there have been limited prior investigations that dealt with the dispersion and settling of firebrands in areas with structures. Of particular interest is when firebrands are deposited in close proximity of structures with the potential of igniting spot fires that burn the structures from the outside. Motivated by this matter and the related recent measurement findings [9] reviewed above, the current computational study is conducted. In Section 2, the mathematical model and the computational approach used in the current simulations are presented. The results are shown and discussed in Section 3, followed by the summary of the work and conclusions in Section 4.

2. Mathematical and computational models

2.1. Firebrand equations

Firebrand equations are expressed and solved in the Lagrangian framework. They are assumed to be rectangular cuboids similar to the firebrands used in the measurements of Suzuki and Manzello [9]. Moreover, they are assumed to keep their mass and shape throughout their motions.

The position and velocity of the firebrand are denoted by \vec{x}_p and \vec{V}_p , respectively, and are governed by

$$\frac{d\vec{x}_p}{dt} = \vec{V}_p, \quad (1)$$

$$m_p \frac{d\vec{V}_p}{dt} = \sum \vec{F}, \quad (2)$$

where d/dt is the time derivative calculated in the Lagrangian framework. Eq. (2) is an expression of Newton's second law where the right hand side is the net force acting on the particle. For the flying firebrand, these are solved in three dimensions with $\sum \vec{F} = \vec{F}_G + \vec{F}_D$ where \vec{F}_D denotes the drag force and \vec{F}_G denotes the gravity combined with the buoyancy force:

$$\vec{F}_G = (\rho_p - \rho_{air}) V \vec{g}, \quad (3)$$

$$\vec{F}_D = \frac{1}{2} C_D \rho_{air} h_p l_p |\vec{V}_{rel}| \vec{V}_{rel}, \quad (4)$$

$$C_D = \frac{8}{Re_p \sqrt{\Phi_{\perp}}} + \frac{16}{Re_p \sqrt{\Phi}} + \frac{3}{\sqrt{Re_p} \Phi^{3/4}} + 0.421^{0.4(-\log(\Phi))^{0.2}} \frac{1}{\Phi_{\perp}}, \quad (5)$$

where ρ_p , h_p , l_p , V , m_p , \vec{V}_{rel} and \vec{g} represent the firebrand density, height, length, volume, mass, velocity of the particle relative to the flow at the particle location, and the gravitational acceleration, respectively.

Here, $\vec{V}_{rel}(t) = \vec{U}(\vec{x}_p(t), t) - \vec{V}_p(t)$ where the first term indicates the flow velocity at the location of the firebrand. In Eq. (5), $Re_p = d_v \rho_{air} |\vec{V}_{rel}| / \mu_{air}$ is the particle Reynolds number where ρ_{air} and μ_{air} are the density and dynamic viscosity of air, respectively. Here, d_v is the diameter of the volume equivalent sphere calculated for the rectangular cuboidal firebrand by

$$d_v = 2 \left(\frac{3 l_p h_p^2}{4\pi} \right)^{1/3}, \quad (6)$$

where $l_p h_p^2$ is the volume of the firebrand, assuming two of the dimensions of the cuboid are identical to h_p , which is consistent with the shape of the firebrands used in the measurements of Suzuki and Manzello [9]. The expression for the drag force in Eq. (4) is attributed to Hölzer and Sommerfeld [18,19] with C_D given in Eq. (5) indicating the drag coefficient, and Φ and Φ_{\perp} representing sphericity and crosswise sphericity, respectively [18]. Here, Φ is defined as the ratio between the surface area of the volume equivalent sphere and the surface area of the firebrand, and the crosswise sphericity Φ_{\perp} is defined as the ratio between the cross-sectional area of the volume equivalent sphere and the projected cross-sectional area of the considered firebrand perpendicular to the flow

$$\Phi = \frac{\pi d_v^2}{2(2h_p l_p + h_p^2)}, \quad (7)$$

$$\Phi_{\perp} = \frac{\pi d_v^2/4}{l_p h_p}. \quad (8)$$

It is assumed that firebrands after landing can slide on the ground with no displacement in the direction normal to the ground. The position and velocity of the sliding firebrand follow Eqs. (1) and (2) in two dimensions on the ground where $\sum \vec{F} = \vec{F}_R + \vec{F}_D$ if $|\vec{F}_D| > |\vec{F}_R|$; otherwise $\vec{V}_p = 0$. Here, \vec{F}_R is the surface friction force acting on the firebrand with the magnitude $|\vec{F}_R| = \mu m_p g$ and the direction opposite to the firebrand velocity. Here, μ denotes the friction coefficient between the firebrand and the ground. In the current study, the static and dynamic friction coefficients were assumed to be identical. The drag force \vec{F}_D here is calculated by Eqs. (4) and (5) with a vanishing component of the relative particle velocity in the direction normal to the ground surface. It is noted, in general, the drag force on the ground will be different from airborne because the flow is bounded on the ground. The examination of this problem can be traced back to O'Neill [20] who considered a spherical particle attached to the wall and derived an analytical solution for the drag force at the very slow flow (creeping) limit. O'Neill's solution resembled the Stokes drag force equation for a spherical particle in a free creeping flow and differed only by a factor 1.7009, i.e., $C_{D,wall} = 1.7009 C_{D,free} = 1.7009 \times 24/Re_p$. Considering the very limited application of the creeping flows, various drag coefficients were formulated in other works [21–23] for a spherical particle near the wall at higher flow velocities. In this formulation, the O'Neill factor 1.7009 was multiplied by the drag coefficients developed through empirical correlations for the spherical particles in free flows with high velocities. Similarly, if the equivalent of the O'Neill factor for rectangular cuboidal particles, considered in the current work, had been known, it would have been multiplied by the C_D given in Eq. (5). In light of this issue, we adopted a unit value for this equivalent factor in an ad hoc manner and applied Eq. (5) also to sliding particles in the present study.

2.2. Computational approach

A model based on the equations discussed in Section 2.1 was developed within the framework of Fire Dynamic Simulator (FDS, version 6.7.0) [24] to simulate the motion of firebrands. To implement the model, the program source of FDS was modified. FDS is open source software designed mainly for simulating fire dynamics and is primarily founded on the computational fluid dynamics (CFD) approaches. It

accounts for various processes involved in fires such as combustion, turbulence, radiation etc. It also includes subroutines to trace particles in the Lagrangian framework. The modification applied on FDS in the current work to simulate firebrands primarily concerned these subroutines. Furthermore, for simulation of the flow in the current work, only the fluid dynamical aspects of FDS was utilized. The low-Mach number flow equations are solved using a second order predictor–corrector scheme in both space and time on a staggered grid. Flow turbulence is dealt with by large eddy simulation (LES) with the Deardoff sub-grid model [25] and the wall-adapting local eddy-viscosity model (WALE) [26] to represent the near-wall effect. It is noted that in LES, a wall model is used to tackle the challenge of fully resolving the flow dynamics near solid boundaries (walls). The computations needed for a full resolution of small flow structures including the boundary layers formed near the wall, are cost prohibitive in general for practical applications as it is the case in the present work. The equations governing the motion of firebrands are solved using a second-order Adams–Bashforth time integration method, as described by Anand et al. [14,15]. The flow solver is coupled with firebrand equations in a one-way manner, which means that the influence of firebrands on the flow is negligible. Moreover, it is assumed that firebrands do not exert any forces on each other.

Firebrands near the ground are subject to the sub-layer and buffer layer effects that are formed on the walls in turbulent flows. However, when a wall model is used, the details of the flow in these regions, such as the sharp wall-normal gradient in the viscous sub-layer, are not resolved. In the present study, to mitigate the accuracy deficit caused by the wall model in representing the near-the-wall-flow effects on firebrands, the modified interpolation scheme suggested by Johnson et al. [27] was implemented by modifying the source code of FDS. This scheme is specifically designed for particles near the wall, where the flow is simulated by LES in conjunction with the wall model. More specifically, the flow velocity at the location of the firebrand is calculated from the flow velocity at the first grid point off the wall using:

$$u_{||}(z_p, t) = f(z^+) u_{||}(z_{1/2}, t), \quad (9)$$

$$f(z^+) = \frac{u^*(z_p^+)}{u^*(z_{1/2}^+)}, \quad (10)$$

where $u_{||}$ indicates the flow velocity component parallel to the wall. Also, z_p denotes the wall-normal coordinates (i.e. z coordinates here) of the firebrand's center of mass and $z_{1/2}$ indicates the z coordinate of the center of the first computational cell off the wall. The superscript $+$ in Eq. (10) indicates the dimensionless wall-normal coordinates. Here, u^* is the dimensionless quantity based on the flow velocity and the friction velocity [27,28] and is given as follows:

$$u^*(z^+) = \ln \left[(z^+ + 4.67)^{2.24} (z^+ - 6.82z^+ + 48.05)^{0.101} \right] + 4.22 \tan^{-1}(0.166z^+ - 0.565) - 1.67. \quad (11)$$

2.3. Overview of simulations

A computational domain of $16 \times 5 \times 13.5$ m (streamwise×spanwise×vertical) resembling the wind tunnel setup of Suzuki and Manzello [9] was constructed in FDS, as displayed in Fig. 1. It is noted that the streamwise, spanwise and vertical directions are indicated by x , y , and z , respectively. The domain was divided into a coarser and a finer grid resolutions. This was done to implement grid stretching in the vertical direction in the lower part of the domain without overstretching the rest of the domain. The coarser grid was uniform with a resolution of $160 \times 50 \times 59$ (streamwise×spanwise×vertical) and was implemented for the top part of the domain, namely from $z = 1.7$ to 13.5 m. The finer grid with the resolution of $320 \times 100 \times 34$ (streamwise×spanwise×vertical) was implemented for the bottom part

of the domain, namely $z = 0$ to 1.7 m. The finer grid was vertically stretched in the direction normal to the ground.

The NIST dragon was represented by a rectangular block with dimensions of $0.3 \times 0.3 \times 1.7$ m (length×width×height) placed one meter from the inlet and two blocks of $2.44 \times 2 \times 2.44$ m (length×width×height) were placed 7.5 m downstream of the dragon mounted to the ground and stuck to the lateral walls of the tunnel. The inlet condition of the domain was set to a uniform wind speed. This parameter was considered with different values $U_w = 4, 6, 8$ and 10 m/s for the analysis of the sensitivity of the results to the wind speed. This set of wind speed values is identical to the one used in the previous experiments [9]. The lateral boundaries were set to be walls. The outlet and top boundaries of the domain were set to be open. Represented in the simulations was the outflow of gases from the mouth of the dragon, reported by Suzuki and Manzello [9] to have a velocity 3 m/s.

After the flow reached a statistically stationary state, firebrands were released from the mouth of the dragon at a rate of 1000 per second in the time interval of $t = 10$ and 30 s. It was verified that turbulence was reached a statistically stationary state before the onset of this time interval. The velocities of the firebrands were not measured in the experiments so in the simulations they were assumed to exit the dragon with a velocity identical to the velocity of the gas exiting from the mouth of dragon, namely 3 m/s. The firebrands had the dimensions of $7.9 \times 7.9 \times 12.5$ mm (length×width×height) and a fixed mass of 0.05 g consistent with the averaged projected area and mass of firebrands reported in the previous measurements [9]. It was stated in this reference that the uncertainties associated with these averaged values were within $\pm 10\%$. In the current simulations, these uncertainties were neglected because: Firstly, the measurement uncertainties within $\pm 10\%$ were assumed negligible since no data such as histograms or numeric distribution were given for the mass and projected area in the measurements which could have been used in the simulations. Secondly, the size and mass variations of the firebrands in the experiments were resulting from their burning, an effect neglected in the current simulations. This neglect is a modeling limitation in the current study. A firebrand mass loss would result in a decrease of the particle response time to the change in the flow velocity condition. As a result, the flow would be more effective in controlling the particle motion. The frictional coefficient between the firebrand and the ground (gypsum board in the experiments) was varied $\mu = 0.5, 0.6$ and 0.7 to investigate the sensitivity of the results to this parameter. A value for the frictional coefficient between a gypsum board and wood was not identified so this range of frictional coefficients, which was reported for the friction between wood and stone [29,30], was chosen here. The simulations were run for a physical time interval of 150 s.

3. Results and discussion

Fig. 2 shows the contour plots and the streamlines of the mean velocity on the planes $y = 0$ and $z = z_{1/2}$, respectively, for a wind speed of $U_w = 10$ m/s. It could be seen in Fig. 2 that on the leeward side of the dragon block, a small re-circulation region (from $x \approx 0$ m to 1.6 m) is formed with lower velocity magnitudes on the ground. The flow separated by the dragon reattaches at $x \approx 1.6$ m on the ground. From there, the flow on the ground seems to diverge but is hindered from diverging further downstream due to the flow re-circulations on the windward sides of the blocks. As the flow re-circulates in this regions, it is funneled towards the gap between the blocks. Streamlines emerge off the windward face of either blocks, but meet each other at $y = 0$ m between $x \approx 6.7$ m to $x \approx 7.5$ m indicating a cross flow in this region (crossflow region). It could be seen in Fig. 2(a) that from $x \approx 6.6$ m, the flow tends to move over a flow structure created by this crossflow on the surface. This prevents the mean flow to stay parallel to the ground between $x \approx 6.7$ m to $x \approx 7.5$ m. The crossflow region potentially acts in opposition to the flow moving through. As the flow advances from the crossflow region, it accelerates, as indicated by the higher

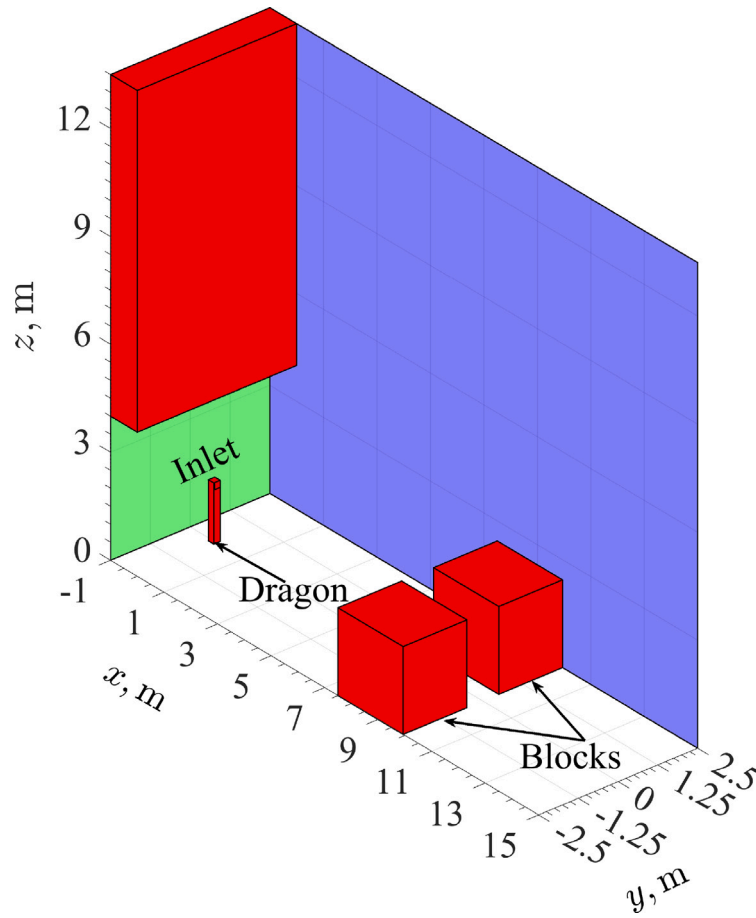


Fig. 1. Computational configuration in the current work based on the experimental setup of [9].

mean velocity in the gap between blocks. After exiting the gap, the flow forms two re-circulating regions on the leeward of the blocks. The flow patterns in other considered wind speeds ($U_w = 4, 6$ and 8 m/s) were overall similar to the ones discussed above for the wind speed of 10 m/s.

In order to determine the significance of the blocks on the flow pattern formed behind the dragon, an additional set of simulations was performed in the same computational configuration where the blocks were removed. The results revealed that the presence of the blocks did not significantly influence the re-circulating region or the flow reattachment on the leeward side of the dragon. However, in the simulations without the blocks, the mean streamlines on the ground surface continued to diverge up to $x \approx 7$ m and were roughly parallel to the lateral wall from the point to the end of the domain whereas the mean streamlines on the plane $y = 0$ were parallel to the surface away from the dragon's wake.

Plotted in Fig. 3 are the dimensionless flow mean velocity and the dimensionless root mean square of the velocity components u_x^{rms}/U_w and u_y^{rms}/U_w vs x at $z = z_{1/2}$. Here, $u_x^{rms} = \sqrt{R_{xx}}$, $u_y^{rms} = \sqrt{R_{yy}}$, and R_{xx} and R_{yy} are the normal components of the Reynolds stress tensor in the x and y directions, respectively. The mean velocity drops on the leeward side of the dragon because of the wake behind the dragon and then peaks at $x \approx 2.8$ m, as shown in Fig. 3(a). This peak corresponds to the reattachment of the flow having been separated by the dragon located upstream. The velocity magnitude drops once more ahead of the blocks at $x \approx 6$ m. Then, it rapidly increases because the flow accelerates at the entrance of the gap between the blocks, where the flow starts converging into the gap (fig. 2 b). Then, the velocity magnitude decreases as the flow decelerates in the x direction. Fig. 3(b) shows that the rms of the flow velocity in the streamwise direction

(solid lines) is higher than that in the spanwise direction (dashed lines) downwind of the dragon except for $x \approx 6.6$ to 7.5 m which corresponds to the crossflow region as noted above. This shows that the spanwise component of velocity has likely more influence in the crossflow region.

It is highly desirable to perform a grid sensitivity analysis in the computational fluid dynamics studies. However, such analysis in LES poses a challenge, as both the sub-grid scale terms in the LES momentum equations and the near-wall model equations are directly dependent on the grid size. As such, the differential equations representing the models themselves change with the change of the grid size and therefore, a rigorous grid sensitivity analysis will not be possible. Nonetheless, in the current work, an additional flow simulation was conducted with a finer grid size of 0.03 m at $U_w = 10$ m/s, noting that the original grid size used in all other simulations was 0.05 m. A figure similar to Fig. 3(a) was generated with two curves based on these two resolutions and they were found to be in close agreement. In light of this finding and the limitation discussed above for grid/mesh sensitivity analysis in LES, it was determined that the lower resolution was adequate in the current study.

Fig. 4 displays top views of the firebrands sliding on the ground under a wind speed of 6 m/s at four different times expressed in the dimensionless form of tU_w/l . Here, $l = 8.5$ m is the distance from the inlet of the domain to the streamwise position windward face of the blocks. Shown in this figure are also the contours of the instantaneous velocity magnitude at $z = z_{1/2}$ m. As could be seen in this figure, firebrands are dispersed much more in the streamwise (x) direction compared to the spanwise (y) direction. The reason for this difference is that the drag force component driving firebrands in the streamwise direction is overall greater than that in the spanwise direction. This is because the streamwise component of the mean flow velocity at

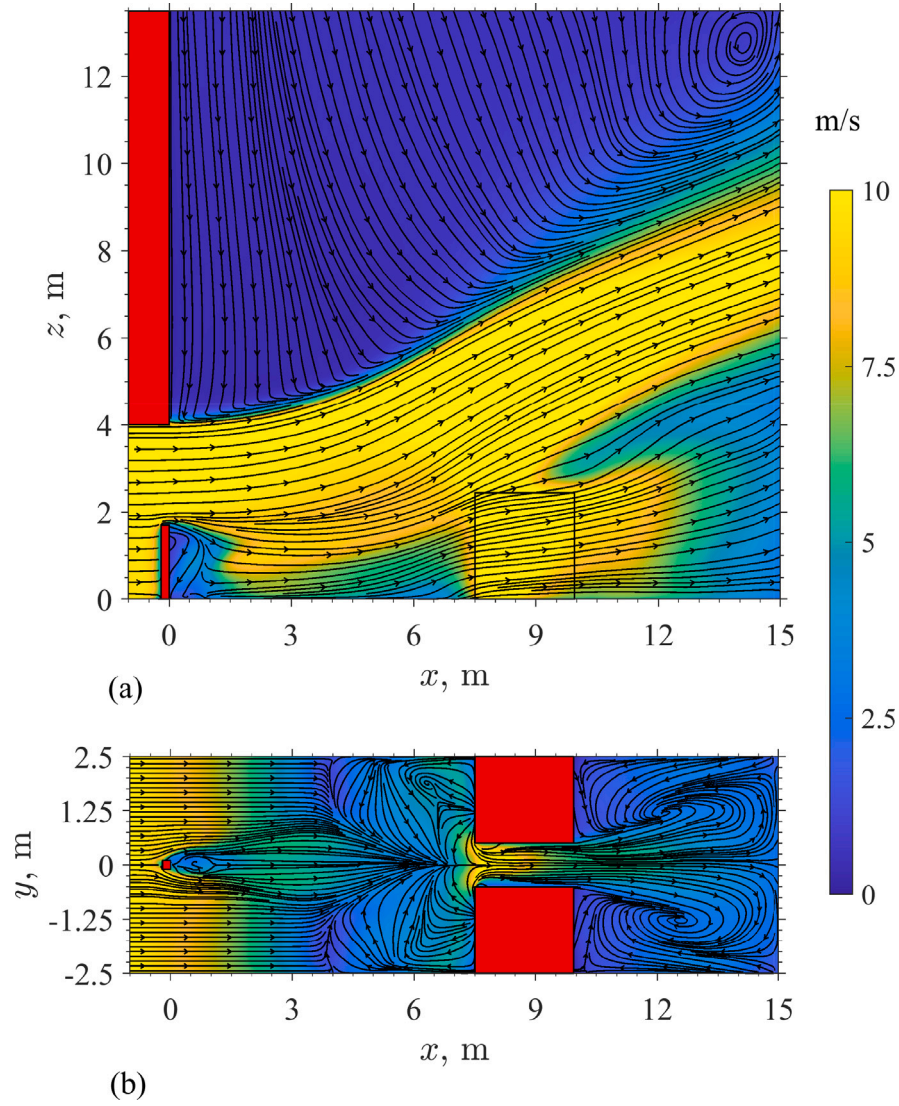


Fig. 2. The contour plots of mean flow velocity and the mean streamlines at (a) $y=0$; and (b) $z=z_{1/2}$ for wind speed of 10 m/s.

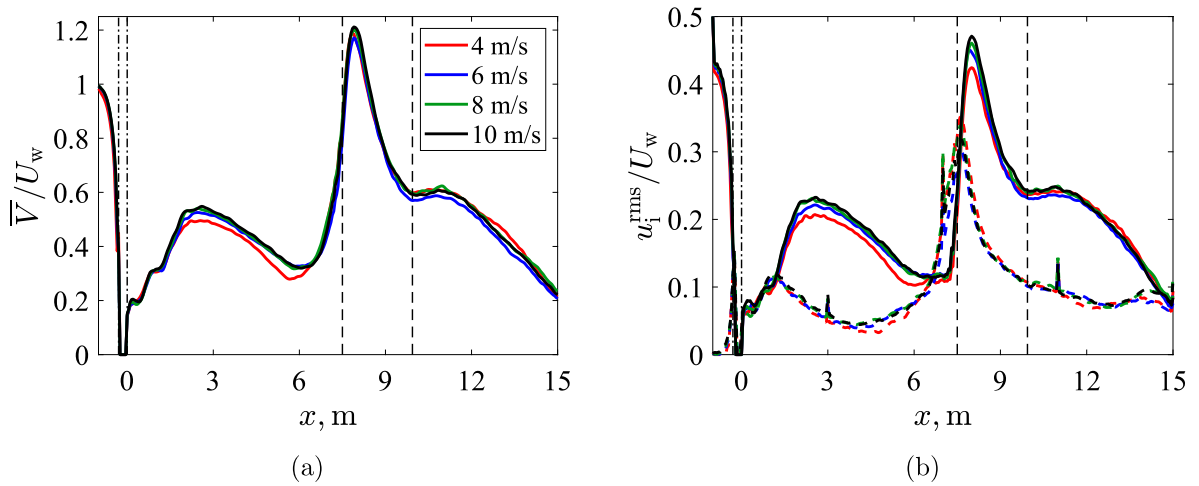


Fig. 3. Dimensionless (a) mean flow velocity magnitude; and (b) rms of the flow velocity components in the streamwise (solid lines) and spanwise (dashed lines) directions at $z=z_{1/2}$ and $y=0$ for varying wind speeds. The location of the dragon and the blocks represented by dashed and dot-dashed lines, respectively.

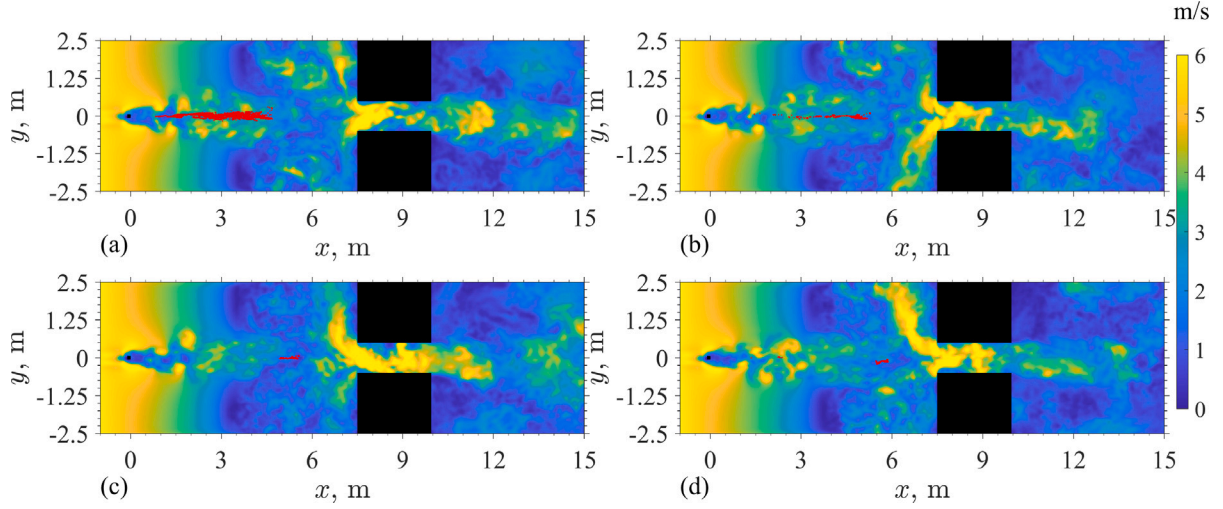


Fig. 4. Scatter plot of firebrands overlaid on contour plot of instantaneous velocity magnitude at $z = z_{1/2}$, for $U_w = 6$ m/s and $\mu = 0.6$ at times (a) $tU_w/l = 28.23$; (b) $tU_w/l = 49.41$; (c) $tU_w/l = 77.64$; and (d) $tU_w/l = 105.87$.

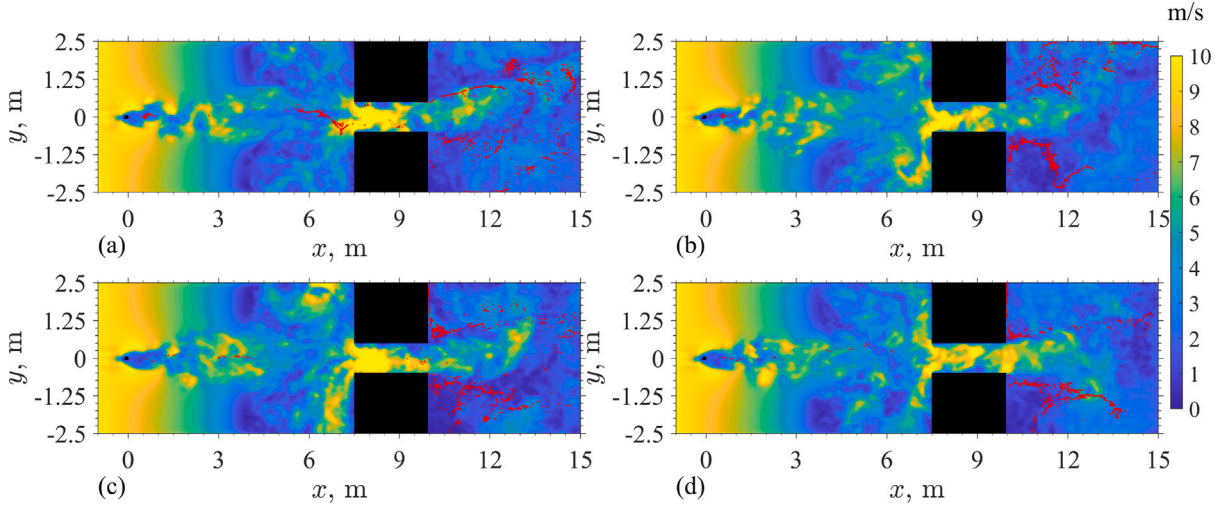


Fig. 5. Scatter plot of firebrands overlaid on contour plot of instantaneous velocity magnitude at $z = z_{1/2}$, for $U_w = 10$ m/s and $\mu = 0.6$ at times (a) $tU_w/l = 82.35$; (b) $tU_w/l = 105$; (c) $tU_w/l = 129.41$; and (d) $tU_w/l = 176.47$.

the locations of firebrands is significantly greater than its spanwise component, as evident from the streamlines shown in Fig. 2(b). Fig. 4 indicates that over time, as the cluster of firebrands slides towards the blocks, the cluster shrinks in the streamwise direction while firebrands converge further to the centerline $y = 0$. A similar behavior was also reported in the previous experiments [9]. The impact of the vortices formed leeward of the dragon on firebrands manifests itself in a slight thickness of the firebrand cluster in the spanwise direction, as could be seen in Fig. 4(a). However, it could be seen in the following subfigures that this thickness diminishes as the cluster slides away from the dragon vortices. Towards the end of the simulations, all the firebrands settle in a small area on the windward side of the blocks right before the crossflow region, as could be seen in Fig. 4(d). The behavior of the firebrands in Fig. 4 during the simulations at a wind speed of 4 m/s exhibited a comparable pattern to that discussed above for the wind speed of 6 m/s, albeit with firebrands settling at a greater distance from the blocks in the lower wind speed.

Fig. 5 displays top views of the firebrands sliding on the ground under a wind speed of 10 m/s at four different times expressed in the dimensionless form of tU_w/l . The firebrand distributions in Fig. 5 exhibit a stark contrast to those in Fig. 4. In all panels in Fig. 5, almost all firebrands have passed through the gap between the blocks and

largely distributed on the leeward of the blocks whereas in Fig. 4, all firebrands are located in the windward of the blocks way ahead of the gap. At this higher wind speed, the flow is characterized by greater values of both average and variance of flow velocities, as could be seen in Fig. 3. Hence, the overall drag force on the firebrands is sufficiently high to drive them towards and through the gap. More specifically, firebrands after deposition tend to follow the mean streamlines between the dragon and the blocks while momentarily accumulating on the windward side of the blocks similar to the previous experiments [9]. However, the firebrands do not settle in this region but rapidly move through the gap. Some firebrands exit the domain as reported in previous experiments [9], while some others end up accumulating towards the leeward edge of the blocks after interacting with the re-circulating regions on the leeward side of the blocks. The simulations reveal that a small number of firebrands are momentarily trapped in the wake of the dragon before sliding towards the blocks. Similar behaviors are observed for a wind speed of $U_w = 8$ m/s.

Fig. 6 shows the range of x coordinates of the settled firebrand clusters (pileups). Such clusters are formed at two wind speeds of 4 and 6 m/s, e.g. Fig. 4(d), but not at the considered higher wind speeds. Fig. 6 includes the data from the previous experiments and the current simulations for various friction coefficients. The x coordinates

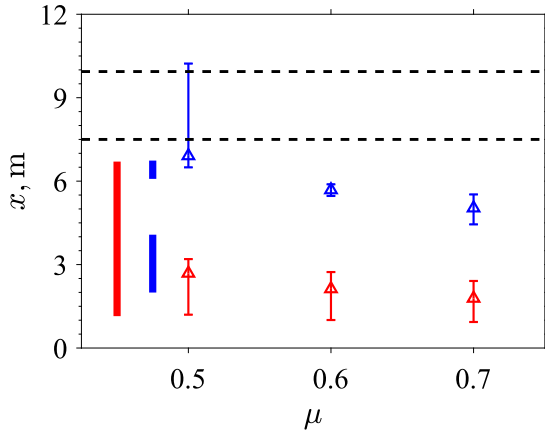


Fig. 6. The mean streamwise position of the accumulated firebrands at the end of the simulation (triangles) at various frictional coefficients for $U_w = 4$ (red), 6 (blue) m/s. The limits of accumulation zones in the present simulation are indicated by error-bars and compared with previous experiments [9] (thick red and blue lines on the left). The horizontal black dashed lines indicate the streamwise locations of the windward and leeward faces of the blocks. (For interpretation of the references to color in this figure legend, the reader is referred to the web version of this article.)

of the windward and leeward faces of the blocks are indicated by solid horizontal black-dashed lines in Fig. 6. The thick solid lines show the data from the measurements of Suzuki and Manzello [9] at wind speeds of $U_w = 4$ and $U_w = 6$ m/s. In the present simulations at $U_w = 4$ m/s, the span of the firebrand cluster ranges from around $x = 1$ m to 4 m for $\mu = 0.5$ and for higher friction coefficients, the span somewhat shortens, as could be seen in Fig. 6. At this wind speed, the firebrand accumulation zone extends from around 1 m to 7 m in the x direction in the previous measurements. At the higher wind speed of 6 m/s, two separate clusters were observed in the previous measurements, as indicated in this figure. The cluster closer to the blocks consisted of a considerably larger number of firebrands and a larger span. In the current simulations, for this wind speed, only one cluster was created as could be seen in Fig. 6 and it was closer to the downwind measured cluster. The span of the simulated cluster was significantly greater than the measured downwind one for $\mu = 0.5$ but for the larger considered friction coefficients were somewhat comparable. In the experiments at wind speed of 6 m/s, it is speculated that the firebrands seen in the cluster closer to the blocks interact with each other and formed a considerable amount of accumulation. This affected the flow upstream of the accumulation region, resulting in a secondary cluster. The neglect of the particle–particle interactions may be the main reason for the current firebrand model not replicating the secondary cluster seen in the experiments. It is also speculated that the absence of the particle–particle interaction in the present simulations results in a shorter span of the particle clusters compared to the experiments at $U_w = 4$ m/s.

Fig. 7 shows the dimensionless velocity magnitude and the dimensionless streamwise position averaged over all firebrands versus dimensionless time $\hat{t}U_w/l$. Defined for each firebrand, \hat{t} indicates the duration that has elapsed since the firebrand was released from the mouth of the dragon, which is the moment the particle tracking started for that firebrand. This elapsed time is calculated by $\hat{t} = t - t_r$ where t_r indicates the release time. Here, $\langle \cdot \rangle$ indicates the ensemble average over firebrands. For example $\langle x_p \rangle$ and $\langle u_p \rangle$ indicate the mean position and velocity of the firebrands in the streamwise direction. For all wind speeds, firebrands on an average deposit in the dragon's wake between $x \approx 1.2$ m and $x \approx 1.5$ m as could be seen in Fig. 2. As firebrands move out of the dragon's wake at $x \approx 1.6$ m, they experience higher flow velocity as the flow separated by the dragon reattaches. This results in an increase in the average firebrand velocity which peaks at $x \approx 2.7$ m corresponding to the peak in the flow velocity as could be seen in

Fig. 3(a). The occurrence of this peak happens at a later time for lower wind speeds and is not observed at $U_w = 4$ m/s. At higher wind speeds $U_w = 8, 10$ m/s, most of the firebrands slow down at $x \approx 5.5$ m as they approach the blocks. This location roughly corresponds to troughs in the flow velocity magnitude displayed in Fig. 3(a). For higher wind speeds, the drag forces are considerably higher than the frictional forces in this region which lead the firebrands to move past the crossflow region and accelerate through the gap, as indicated by the second peak in Fig. 7(a). However, for lower wind speeds of $U_w = 4$ and 6 m/s, the firebrands tend to slow down and settle on the windward side of the blocks. The reason for this settlement is the dominance of the frictional forces over the drag forces in this regions. For higher wind speeds of $U_w = 8, 10$ m/s, the modification in the interpolation model causes the firebrands to experience a lower fluid velocity causing the firebrands to reach the gap later and consequently accelerating later. This delays the second peak seen in the averaged velocity for higher wind speeds. In case of $U_w = 6$ m/s, the drag force is not large enough to make firebrands move past the gap. Also the average streamwise position of the firebrands at $U_w = 4$ m/s is lower when the interpolation model is modified as compared to the same speed without the interpolation modification.

Plotted in Fig. 8 are the dimensionless variances of the firebrand positions in the streamwise and spanwise directions, respectively, versus dimensionless time $\hat{t}U_w/l$. If the firebrand position fluctuations are defined and indicated by $x'_p = x_p - \langle x_p \rangle$ and $y'_p = y_p - \langle y_p \rangle$ in the streamwise and spanwise directions, respectively, the firebrand position variances are defined and denoted by $\langle x'_p x'_p \rangle / l^2$ and $\langle y'_p y'_p \rangle / l^2$. These are indicative of the dispersion of firebrands in the streamwise and spanwise directions, respectively. Comparing panel (a,c) vs panel (b,d) in Fig. 8 shows that, overall, $\langle x'_p x'_p \rangle / l^2$ is greater than $\langle y'_p y'_p \rangle / l^2$ at a given time and wind speed. This means that overall, firebrands are more widely dispersed in the streamwise direction compared to the spanwise direction. This difference is attributed to the fact that the rms of the flow velocity component in the streamwise direction is greater than that in the spanwise direction, as could be seen in Fig. 3(b).

As seen in Fig. 8(a,b), $\langle x'_p x'_p \rangle / l^2$ and $\langle y'_p y'_p \rangle / l^2$ are orders of magnitude smaller at wind speeds of 4 and 6 m/s as compared to higher wind speeds. This is a consequence of lower values of both average and variance of flow velocities at lower wind speeds (Fig. 3). At $\hat{t}U_w/l \approx 10$ for wind speeds of 6 m/s, the value of $\langle x'_p x'_p \rangle / l^2$ peaks, which roughly corresponds to the peak in the average flow velocity and its variance in the streamwise direction at $x \approx 2.8$ (Fig. 3). This peak is, however, absent at the wind speed of 4 m/s since most firebrands accumulate before $x \approx 2.8$, as could be seen in Fig. 6. On the other hand, the value of $\langle y'_p y'_p \rangle / l^2$ decreases after the firebrands deposit on the surface for these wind speeds. This decrease indicates that the firebrand cluster is less dispersed in the spanwise direction (Fig. 4).

Examining Fig. 8(c,d) reveals that at the wind speed of 8 m/s, $\langle y'_p y'_p \rangle / l^2$ has a negligible value for $\hat{t}U_w/l < 23$ and then increases rapidly. Within this time interval, $\langle x'_p x'_p \rangle / l^2$ displays an initial increase after firebrands' deposition on the ground and then plateaus at ~ 0.027 m². At $\hat{t}U_w/l \approx 23$, $\langle x_p \rangle$ is around 6 m, which is 1.5 m upwind of the windward side of the blocks according to Fig. 7(b). These findings suggest that particles are mostly located upwind of the blocks with little dispersion in the spanwise direction and somewhat dispersion in the streamwise direction at wind speed of 8 m/s for $\hat{t}U_w/l < 23$. After this time, both $\langle x'_p x'_p \rangle / l^2$ and $\langle y'_p y'_p \rangle / l^2$ rapidly increase, as a result of firebrands encountering the recirculating flow windward of the blocks, as could be seen in Fig. 2(b). While $\langle x'_p x'_p \rangle / l^2$ plateaus at $\hat{t}U_w/l \approx 28$, $\langle y'_p y'_p \rangle / l^2$ keeps increasing until $\hat{t}U_w/l \approx 56$. This is the time when particles have mostly moved to the leeward of the blocks and mixed by the vortices formed behind them. Two major factors contribute to this rapid increase of $\langle y'_p y'_p \rangle / l^2$: First, the bifurcation of the positions of the most of the firebrands that exit the gap between the blocks, as some shift towards the leeward of one block and some others shift towards the leeward of the other block. This phenomenon is correlated with the

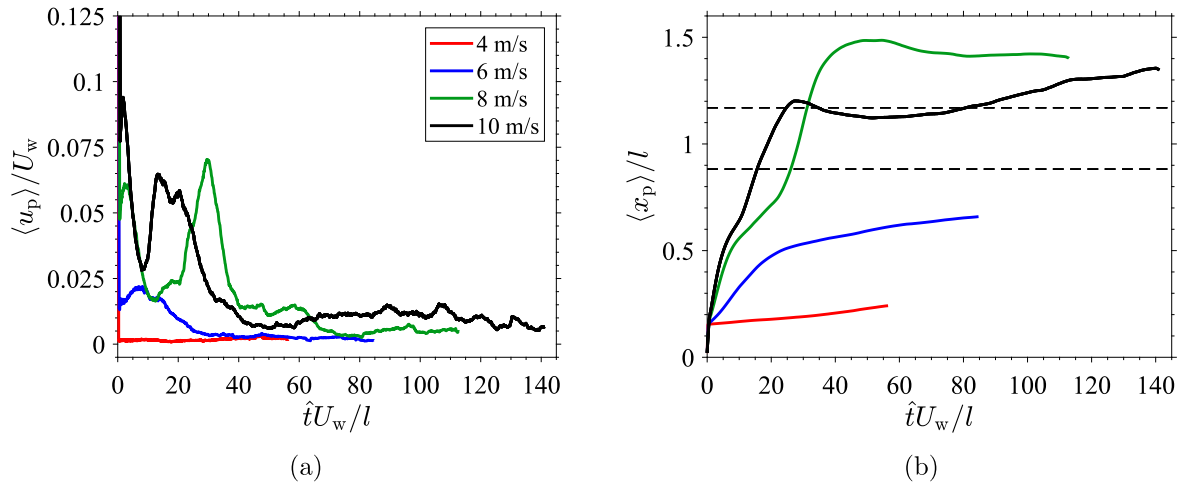


Fig. 7. Mean firebrand velocity (panel a) and position (panel b) in the streamwise directions vs $\hat{t}U_w/l$ for $\mu = 0.6$. The blocks are located between the dashed lines.

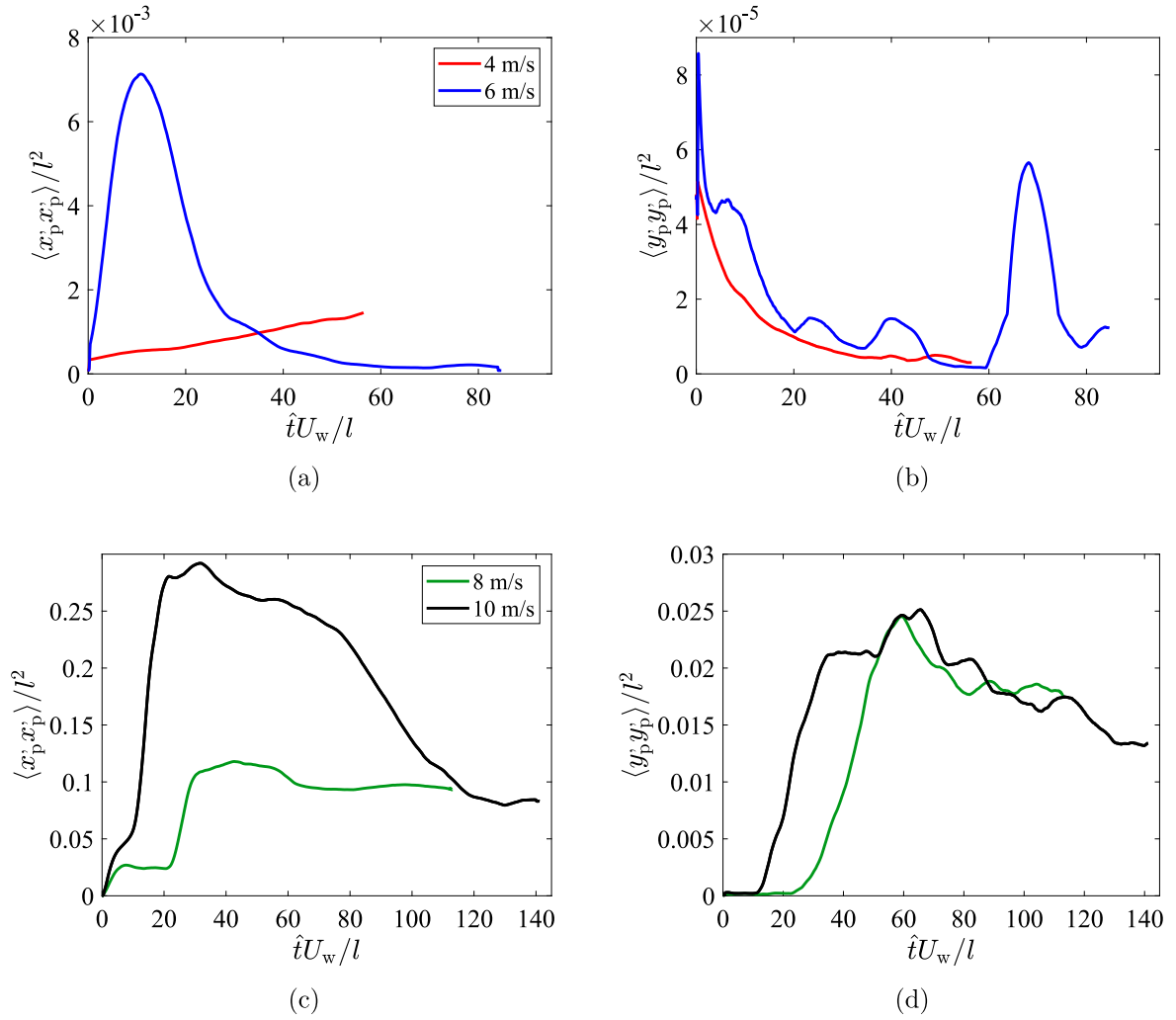


Fig. 8. The variance of the firebrand positions in streamwise (left column); and spanwise (right column) directions for $\mu = 0.6$ versus $\hat{t}U_w/l$.

two main vortices formed behind the two blocks (Fig. 2). Second, some firebrands temporarily trap in the corners between the ground and the leeward faces of the blocks, aligning in the y direction, as could be seen in Fig. 5(c,d). At elevated wind speeds of 8 and 10 m/s, there is a marked increase in the variances in both streamwise and spanwise directions as the firebrands approach and move past the blocks. On the other hand, at lower wind speeds of 4 and 6 m/s, the firebrands never approach the blocks closely, resulting in consistently low variances.

4. Summary and conclusions

The tracking of firebrands was modeled in the Lagrangian framework in both airborne mode under the drag and gravity forces and sliding mode under the drag and frictional forces on the ground. This was achieved by changing the source code of FDS and utilizing it to simulate the flow by LES coupled with the Lagrangian modeling of firebrands. The change was made to include the sliding motion of the firebrands on the ground, the rectangular cuboidal shape for firebrands and the corresponding drag force, and the modified interpolation scheme near the wall to represent the effect of the viscous sub-layer on sliding firebrands, as a wall model was used with LES. The modeling was conducted in a computational configuration resembling a previous experimental setup [9]. It was an open circuit wind tunnel including an apparatus (a.k.a NIST Dragon) whereby firebrands were produced and released from a location about 1.6 m off the ground and deposited upwind of two parallel blocks. The blocks had a size of $2.44 \times 2 \times 2.44$ m (length \times width \times height), separated by a one meter gap. The size of firebrands was $7.9 \times 7.9 \times 12.5$ mm.

The flow simulations were conducted for wind speeds of 4, 6, 8 and 10 m/s. They displayed similar overall flow features including re-circulation zones on the dragon's leeward, and the leeward of the blocks. Additionally, a crossflow area located on the windward side of the blocks was identified, which created a crossflow to the incoming flow towards the gap between the blocks. Following a brief moment of landing after release from the dragon's mouth, firebrands transitioned into the sliding mode of motion on the ground. They landed in the wake region of the dragon and then slid downward towards the gap between the blocks. At higher simulated wind speeds of 8 and 10 m/s, a higher mean velocity of the flow was identified as it traversed the gap causing the firebrands to accelerate while moving in the gap. At these wind speeds, firebrands momentarily accumulated and slowed down on the windward of the blocks before accelerating in the gap and then recirculating on the leeward of the blocks. Firebrands displayed an increasing variance of the streamwise position of firebrands, as they move out of the dragon's wake. At lower simulated wind speeds of 4 and 6 m/s, firebrands settled before reaching the gap, forming a cluster of accumulated firebrands. A similar behavior was also reported in the previous experiments although the simulated cluster size was found smaller than that measured in the previous experiments. Overall, the dispersion of firebrands, as quantified by the variances of the positions of moving firebrands, was found to be much more in the streamwise direction compared to the spanwise direction. This difference was attributed to the fact that the variance of the flow velocity component in the streamwise direction was greater than the spanwise direction. At higher wind speeds after firebrands passed through the gap between the blocks, the variance of the firebrand position in the spanwise direction gained a significant increase as a result of the bifurcation of the firebrand positions, as some firebrands were circulated by the main vortex formed in the leeward of one block while some others were circulated by the main vortex formed in the leeward of the other block. Another factor contributing to this increase was the temporary trapping of some firebrands in the corners between the ground and the leeward faces of the blocks.

CRediT authorship contribution statement

Aditya Mankame: Writing – original draft, Visualization, Validation, Software, Methodology, Investigation, Formal analysis, Data curation, Conceptualization. **Patrick Damiani:** Visualization, Software, Methodology, Formal analysis. **Babak Shotorban:** Writing – original draft, Writing – review & editing, Validation, Supervision, Resources, Project administration, Methodology, Investigation, Funding acquisition, Formal analysis, Data curation, Conceptualization.

Declaration of competing interest

The authors declare that they have no known competing financial interests or personal relationships that could have appeared to influence the work reported in this paper.

Data availability

Data will be made available on request.

Acknowledgments

The authors acknowledge the useful discussions with S. L. Manzello and S. Suzuki, pertinent to their work [9]. The current work was in part performed under the financial assistance award 70NANB17H281 from U.S. Department of Commerce, National Institute of Standards and Technology. High performance computing resources and technical support from the Alabama Supercomputer Authority were appreciated.

References

- [1] C.S. Tarifa, P.P. del Notario, F.G. Moreno, Transport and Combustion of Fire Brands, Instituto Nacional de Tecnica Aeroespacial, "Esteban Terradas", 1967.
- [2] N. Sardoy, J. Consalvi, A. Kaiss, A. Fernandez-Pello, B. Porterie, Numerical study of ground-level distribution of firebrands generated by line fires, *Combust. Flame* 154 (3) (2008) 478–488.
- [3] E. Koo, P.J. Pagni, D.R. Weise, J.P. Woycheese, Firebrands and spotting ignition in large-scale fires, *Int. J. Wildland Fire* 19 (7) (2010) 818–843.
- [4] R. Bianchi, J.E. Leonard, R.H. Leicester, Lessons learnt from post-bushfire surveys at the urban interface in Australia, *Forest Ecol. Manag.* 234 (1) (2006) S139.
- [5] S.L. Manzello, S. Suzuki, Exposing decking assemblies to continuous wind-driven firebrand showers, *Fire Safety Sci.* 11 (2014) 1339–1352.
- [6] S. Suzuki, S.L. Manzello, K. Kagiya, J. Suzuki, Y. Hayashi, Ignition of mulch beds exposed to continuous wind-driven firebrand showers, *Fire Technol.* 51 (2015) 905–922.
- [7] S.L. Manzello, S. Suzuki, D. Nii, Full-scale experimental investigation to quantify building component ignition vulnerability from mulch beds attacked by firebrand showers, *Fire Technol.* 53 (2017) 535–551.
- [8] S. Suzuki, S.L. Manzello, Ignition vulnerabilities of combustibles around houses to firebrand showers: further comparison of experiments, *Sustainability* 13 (4) (2021) 2136.
- [9] S. Suzuki, S.L. Manzello, Investigating the effect of structure to structure separation distance on firebrand accumulation, *Front. Mech. Eng.* 6 (2021) 628510.
- [10] A. Tohidi, N.B. Kaye, Comprehensive wind tunnel experiments of lofting and downwind transport of non-combusting rod-like model firebrands during firebrand shower scenarios, *Fire Saf. J.* 90 (2017) 95–111.
- [11] A. Tohidi, N.B. Kaye, Stochastic modeling of firebrand shower scenarios, *Fire Saf. J.* 91 (2017) 91–102.
- [12] D. Nguyen, N.B. Kaye, Quantification of ember accumulation on the rooftops of isolated buildings in an ember storm, *Fire Saf. J.* 128 (2022) 103525.
- [13] D. Nguyen, N.B. Kaye, The role of surrounding buildings on the accumulation of embers on rooftops during an ember storm, *Fire Saf. J.* (2022) 103624.
- [14] C. Anand, B. Shotorban, S. Mahalingam, Dispersion and deposition of firebrands in a turbulent boundary layer, *Int. J. Multiph. Flow* 109 (2018) 98–113.
- [15] C. Anand, Computational Investigations of Ignition Characteristics of Live Fuels and Deposition of Firebrands in a Turbulent Boundary Layer (Ph.D. thesis), The University of Alabama in Huntsville, 2018.
- [16] A. Mankame, B. Shotorban, Deposition characteristics of firebrands on and around rectangular cubic structures, *Front. Mech. Eng.* 7:640979 (2021) 53.
- [17] A. Mankame, B. Shotorban, Firebrand deposition on cubic structures in tandem and parallel arrangements, *Int. J. Multiph. Flow* 168 (2023) 104578.
- [18] A. Hölzer, M. Sommerfeld, New simple correlation formula for the drag coefficient of non-spherical particles, *Powder Technol.* 184 (3) (2008) 361–365.

- [19] G. Bagheri, C. Bonadonna, On the drag of freely falling non-spherical particles, *Powder Technol.* 301 (2016) 526–544.
- [20] M. O'Neill, A sphere in contact with a plane wall in a slow linear shear flow, *Chem. Eng. Sci.* 23 (11) (1968) 1293–1298.
- [21] L. Sweeney, W. Finlay, Lift and drag forces on a sphere attached to a wall in a Blasius boundary layer, *J. Aerosol Sci.* 38 (1) (2007) 131–135.
- [22] A. Ibrahim, P. Dunn, M. Qazi, Experiments and validation of a model for microparticle detachment from a surface by turbulent air flow, *J. Aerosol Sci.* 39 (8) (2008) 645–656.
- [23] C.-N. Liu, C.-L. Chien, C.-C. Lo, G.-Y. Lin, S.-C. Chen, C.-J. Tsai, et al., Drag coefficient of a spherical particle attached on the flat surface, *Aerosol Air Qual. Res.* 11 (5) (2011) 482–486.
- [24] K. McGrattan, S. Hostikka, J. Floyd, R. McDermott, M. Vanella, *Fire Dynamics Simulator Technical Reference Guide Volume 1: Mathematical Model*, NIST Special Publication- Sixth Edition 1018-6, U.S. Department of Commerce, National Institute of Standards and Technology, 2018.
- [25] J.W. Deardorff, Stratocumulus-capped mixed layers derived from a three-dimensional model, *Bound.-Layer Meteorol.* 18 (4) (1980) 495–527.
- [26] F. Nicoud, F. Ducros, Subgrid-scale stress modelling based on the square of the velocity gradient tensor, *Flow Turbul. Combust.* 62 (3) (1999) 183–200.
- [27] P.L. Johnson, M. Bassenne, P. Moin, Turbophoresis of small inertial particles: theoretical considerations and application to wall-modelled large-eddy simulations, *J. Fluid Mech.* 883 (2020) A27, 1–38.
- [28] A. Liakopoulos, Explicit representations of the complete velocity profile in a turbulent boundary layer, *AIAA J.* 22 (6) (1984) 844–846.
- [29] J. Aira, F. Arriaga, G. Íñiguez-González, J. Crespo, Static and kinetic friction coefficients of Scots pine (*Pinus sylvestris* L.), parallel and perpendicular to grain direction, *Mater. Construcción* 64 (315) (2014) e030, 1–8.
- [30] H. Al Qablan, S. Rababeh, H. Katkhuda, T. Al-Qablan, On the use of wooden beams as an anti-seismic device in stone masonry in Qasr el-Bint, Petra, Jordan, *J. Build. Eng.* 21 (2019) 82–96.